

# JGR Atmospheres

## RESEARCH ARTICLE

10.1029/2019JD031848

### Key Points:

- During periods of large-scale subsidence in the Eastern North Atlantic, rain properties are strongly related to cloud thickness even in ice-topped clouds
- Likely because of their relationship to cloud thickness, surface forcing and boundary layer stability impact rain fraction and rain rate
- Post-cold frontal shallow clouds precipitate more frequently and have a higher rain-to-cloud fraction than clouds in general subsidence

### Supporting Information:

- Supporting Information S1
- Figure S1
- Figure S2

### Correspondence to:

K. Lamer,  
klamer@bnl.gov

### Citation:

Lamer, K., Naud, C. M., & Booth, J. F. (2020). Relationships between precipitation properties and large-scale conditions during subsidence at the Eastern North Atlantic observatory. *Journal of Geophysical Research: Atmospheres*, 124. <https://doi.org/10.1029/2019JD031848>

Received 16 OCT 2019

Accepted 18 MAR 2020

Accepted article online 20 MAR 2020

### Author Contributions:

**Conceptualization:** Katia Lamer, Catherine M. Naud, James F. Booth

**Formal analysis:** Katia Lamer

**Funding acquisition:** Catherine M. Naud, James F. Booth

**Investigation:** Katia Lamer

**Methodology:** Katia Lamer, Catherine M. Naud, James F. Booth

**Supervision:** Catherine M. Naud, James F. Booth

**Visualization:** Katia Lamer

**Writing - original draft:** Katia Lamer

**Writing - review & editing:**

Catherine M. Naud, James F. Booth

## Relationships Between Precipitation Properties and Large-Scale Conditions During Subsidence at the Eastern North Atlantic Observatory

Katia Lamer<sup>1,4</sup> , Catherine M. Naud<sup>2</sup> , and James F. Booth<sup>1,3</sup> 

<sup>1</sup>Earth and Atmospheric Sciences, The City University of New York, City College New York, NY, USA, <sup>2</sup>Applied Physics and Applied Mathematics, Columbia University/NASA-GISS, New York, NY, USA, <sup>3</sup>The Graduate Center, City University of New York, New York, NY, USA, <sup>4</sup>Now at the Department of Environmental and Climate Sciences, Brookhaven National Laboratory, Upton, NY, USA

**Abstract** Three years of reanalysis and ground-based observations collected at the Eastern North Atlantic (ENA) observatory are analyzed to document the properties of rain and boundary layer clouds and their relationship with the large-scale environment during general subsidence conditions and following cold front passages. Clouds in the wake of cold fronts exhibit on average a 10% higher propensity to precipitate and higher rain-to-cloud fraction than cloud found in general subsidence conditions. Similarities in the seasonal cycle of rain and of large-scale properties suggest that the large-scale conditions created by the cold front passage are responsible for the unique properties of the rain forming in its wake. The identification of monotonic relationships between rain-to-cloud fraction and rain rate with surface forcing and boundary layer stability parameters as well as between virga base height with stability and humidity measures further supports that large-scale conditions impact precipitation variability. That being said, these relationships between the large-scale and rain properties are less clear than those established between cloud and rain properties, suggesting that cloud microphysics have a more direct impact on the properties of rain than the large-scale environment. The applicability of previously documented relationships between cloud thickness and rain properties is tested and the relationships adjusted to accommodate the complex shallow clouds and melting precipitation observed to occur in the ENA region. Establishing these relationships opens up opportunities for parametrization development and suggests that a realistic representation of precipitation properties in models relies on the accurate representation of both clouds and the large-scale environment.

## 1. Introduction

Reports of disagreements between numerically modeled and observed rain frequency and intensity (e.g., Kay et al., 2018; Naud et al., 2020; Stephens et al., 2010; Sun et al., 2006) suggest that it remains challenging to simulate rain in large-scale models. Particular challenges have been identified with the representation of clouds and precipitation in post-cold frontal (PCF) conditions (Bodas-Salcedo et al., 2012; Bodas-Salcedo et al., 2014; Naud et al., 2014, 2020). PCF regions are marked by complex combinations of stratocumulus and cumulus clouds (Lau & Crane, 1997), which commonly precipitate (Leon et al., 2008; Rémillard et al., 2012; Zhou et al., 2015).

Observations have revealed that precipitation influences both the cloud field and the environment in many ways. For instance, inside clouds, precipitation formation alters the drop size distribution (Wood et al., 2012) and is believed to impact cloud lifetime (Paluch & Lenschow, 1991). As it exits the cloud layer and enters the subcloud layer, depending on whether or not it reaches the surface, precipitation either affects the surface hydrological cycle or generates evaporative cold pools believed to lead to cloud mesoscale organization (e.g., Savic-Jovicic & Stevens, 2008; Wang & Feingold, 2009; Yamaguchi & Feingold, 2015; Zhou et al., 2017; Zhou et al., 2018). Since most of these precipitation processes ultimately affect the radiative budget, it is crucial for them to be accurately represented in large-scale climate models.

Although the treatment of precipitation in numerical models has progressed in the last decade (for example, transition from diagnostic (Morrison & Gettelman, 2008) to prognostic (Gettelman & Morrison, 2015) schemes), it remains simplified because it is associated with processes occurring at scales smaller than the

model resolution. Examples of simplifications include parametrizing the horizontal area coverage of rain as a function of cloud area coverage (i.e., rain-to-cloud fraction [RCF]; e.g., Ahlgrimm & Forbes, 2014; Rotstayn, 1997) or determining when evaporation takes place using tunable critical relative humidity thresholds (Ahlgrimm, personal communication, February 14, 2019). Improving our understanding of the factors controlling precipitation and its properties including rain rate, RCF and virga base height could contribute to improving existing parametrizations and ultimately rain and climate prediction.

Previous observational studies suggest that, following precipitation onset, precipitation properties are much more sensitive to changes in cloud macrophysical properties (cloud thickness and liquid water path) than to changes in cloud microphysics (effective radius and effective droplet number concentration) (Kubar et al., 2009). This idea is further supported by evidence that, among other precipitation properties, rain rate ( $RR$ ) scales with a factor of 3 of cloud thickness ( $H$ ) while only being inversely proportional to droplet number concentration ( $N$ ; i.e.,  $RR \sim H^3/N$ ) (VanZanten et al., 2005; Yang et al., 2018). Since a recent study by Naud et al. (2018) points out that cloud macrophysical properties, including cloud thickness, are largely influenced by large-scale conditions, it would not be surprising for rain characteristics to also be influenced by the properties of the large-scale environment in which they form. That may be especially the case in subsidence regimes where clouds are confined to the shallow boundary layer. In a recent study, Wu et al. (2017) presented evidence that precipitation rate may be affected by environmental turbulence especially under stable conditions; if other precipitation properties are affected by environmental stability, turbulence, or other large-scale properties such as surface forcing and thermodynamic state, then deficiencies in simulated large-scale properties could also account for some of the biases identified in global numerical simulations.

With this as motivation, the present study uses a combination of reanalysis and ground-based observations collected over 3 years (2015–2018) at the Atmospheric Radiation Measurement (ARM) program's Eastern North Atlantic (ENA) facility to

1. provide new sets of observational benchmarks useful for evaluating the properties of numerically modeled rain, focusing on subsidence conditions following the passage of a cold front, which are known to be particularly challenging to represent;
2. provide information to improve/build new parametrizations by identifying the properties that drive changes in precipitation characteristics. This includes evaluating how cloud thickness, cloud microphysical phase, environmental stability, and surface forcing parameters affect rain rate, RCF, and virga base height.

## 2. Data Sets and Methodology

Between October 2015 and September 2018, the ARM program operated an observatory in the ENA on the island of Graciosa (39.1°N, 28.0°W) (Wood et al., 2015). Graciosa island is the northmost island of the Azores Archipelago and is relatively small (~12 km across) and flat (highest peak 400 m); as such, it is expected that the sensors deployed on the northern edge of the island collect measurements representative of oceanic conditions, marginally impacted by the island's influence especially under northerly flow.

Graciosa island straddles the boundary between the subtropics and the midlatitudes and as such is subject to a wide range of meteorological conditions (Rémillard & Tselioudis, 2015). This analysis capitalizes on observations to characterize periods of subsidence and especially those occurring following the passage of a cold front as identified using a combination of observations and Modern-Era Retrospective analysis for Research and Applications version 2 (MERRA-2) reanalysis (Gelaro et al., 2017) (section 2.1). The intent of this study is to characterize oceanic precipitation (section 2.2), and its associated clouds (section 2.2) and large-scale conditions (section 2.3), and to identify which cloud or large-scale property(ies) could explain observed variations in rain properties (section 2.4). Data availability is discussed in section 2.5.

### 2.1. Identification of Cold Frontal and Subsidence Conditions With Northerly Wind

This analysis focuses on subsidence conditions defined as 1-hr periods exhibiting downward vertical motion at 500 hPa (i.e.,  $\omega_{500} > 0$  hPa hr<sup>-1</sup>), which we identify using vertical velocity from the 0.5° × 0.625° spatial resolution MERRA-2 1-hourly, time-averaged, single-level, assimilation reanalysis product (M2T1NXSLV V5.12.4). We further identify subsidence conditions resulting from the passage of a cold front (hereafter referred to as “post-cold frontal” or PCF) and separate them from those not associated with a front

(hereafter referred to as “general subsidence” or non-PCF). General subsidence conditions do not include conditions of northwesterly winds to avoid possible contamination by non-identified cold fronts. Conditions with southerly winds are also systematically discarded to avoid possible island effects. Most vulnerable to island effects are observations collected by in situ surface sensors. In the current study those include temperature and relative humidity measured by the meteorological station, which might be affected by daytime surface heating.

Cold fronts are identified following the approach described in Naud et al. (2018). In a nutshell, the Modeling, Analysis, and Prediction (MAP) Program Climatology of Midlatitude Storminess (MCMS; Bauer & Del Genio, 2006) cyclone location algorithm is used to identify extratropical cyclones that travel in the North Atlantic. Fronts associated with these cyclones are identified using potential temperature gradients and wind direction changes estimated from the  $0.5^\circ \times 0.625^\circ$  spatial resolution MERRA-2 6-hourly, instantaneous, analyzed meteorological fields (M2I6NPANA V5.12.4). Frontal passage over the ENA observatory is confirmed through the identification of a shift in surface wind direction from southerly to northerly at the observatory (using the meteorological station). In this study, PCF events are taken to start at the time of this wind direction shift and end at the time when the wind becomes southerly again.

## 2.2. Observations and Retrieval of Precipitation and Cloud Properties

Observations collected by the second generation Ka-band ARM Zenith Radar (KAZR2; enakazrgeC1.a1) and the Vaisala Ceilometer lidar (enaceilC1.b1) are noise and clutter filtered, calibrated, and combined to characterize cloud and precipitation at 30-m, 2-s spatiotemporal resolution at all heights between 60 m and 4 km above the surface where both sensors record signals above their detection limit (Kollias et al., 2019; Lamer et al., 2019). The maximum height of 4 km is selected to maintain our focus on marine boundary layer clouds; to avoid contamination from deep clouds extending beyond the boundary layer or midlevel clouds precipitating in the boundary layer, hourly periods that include more than 1-min worth of radar reflectivity echoes at 4 km are not used in this analysis.

The 2-s resolution observations are aggregated in 1-hr windows to facilitate the examination of all observations in the context of large-scale conditions. However, to conserve the high-resolution information of the original measurements, all precipitation and cloud characteristics are first estimated at the native 2-s resolution of the measurements and then averaged over the 1-hr windows. Figure 1 shows an example radar reflectivity observations and cloud properties retrieved at the native time resolution of the measurements collected in the wake of a cold front that passed the ENA observatory on 8 April 2016.

### 2.2.1. Melting-Layer Identification

Because liquid and frozen hydrometeors differently affect radar and lidar signals, we begin our characterization of the cloud field by employing a melting layer detection technique. Similar to others before, we identify the melting layer height using radar linear depolarization ratio (LDR) measurements (Sandford et al., 2017): First, every hour, the height of the  $0^\circ$  C isotherm is approximated using the closest in time sounding; then a melting layer is identified if, within 1 km from the  $0^\circ$  C isotherm, the profile of hourly maximum LDR presents both an LDR peak at least 2 dB larger than the neighboring values in height as well as an LDR gradient larger than  $15 \text{ dB km}^{-1}$ . For example, melting layers were identified for all hourly periods between 23:00 UTC on 10 April 2016 and 16:00 UTC on 11 April 2016 (Figure 1).

### 2.2.2. Cloud Characteristics

Any radar echo detected above a lidar-identified cloud base is labeled as “cloud.” To account for ice clouds that may not be detected by the lidar, radar echoes detected above the melting layer (if any) are also identified as “cloud.”

- Cloud top height: Cloud top is defined as the highest cloud echo below 4 km. Examples of high-resolution cloud top height identifications used to estimate the hourly average cloud top height are depicted in Figure 1.
- Cloud base height: The lidar-identified first cloud base height is used as an initial measure of cloud base height. This initial measure is adjusted (1) to account for lidar signal attenuation by rain—ceilometer estimates coinciding with a radar reflectivity larger than  $-5 \text{ dBZ}$  (a signature for rain) are replaced by the closest in time (within the hour) valid lidar-identified first cloud base height (examples in Figure 1)—and (2) to account for melting layers below the lidar detected first cloud base height—if the initial

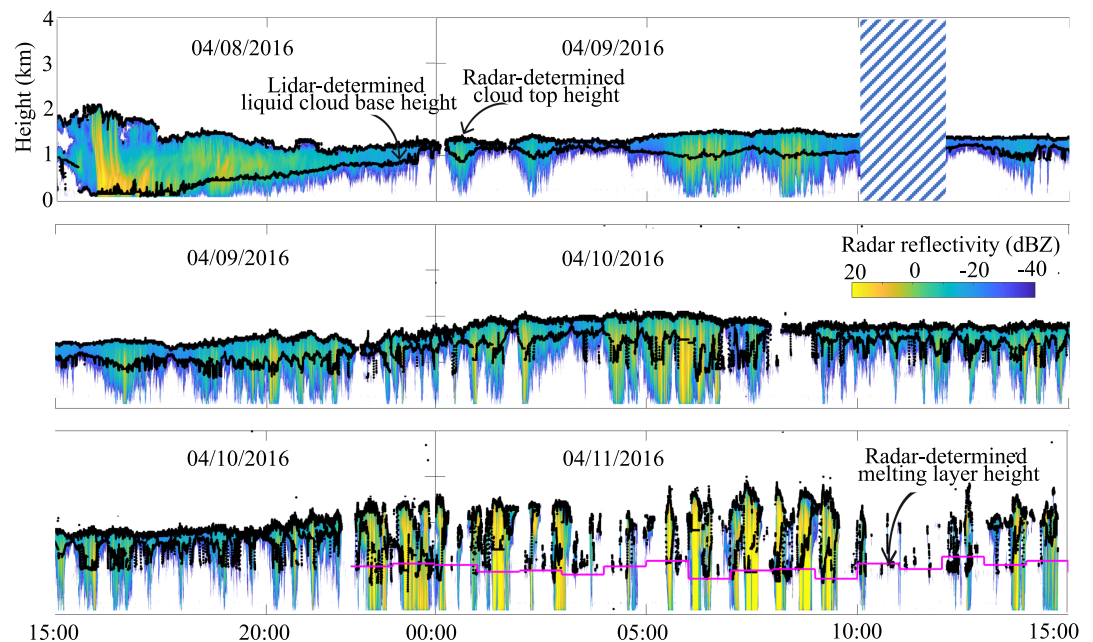


**Figure 1.** Time series of radar reflectivity measured at the ENA facility following the passage of a cold front on 8 April 2016. Also plotted are the lidar-determined cloud base height (lowest set of black dots), the radar-determined cloud top (highest set of black dots), and the melting layer (magenta line). The hatched region marks a period of missing data.

measure of cloud base height provided by the lidar is above the radar detected melting layer, the radar-detected melting layer height is used instead as the measure of cloud base height.

- **Cloud thickness:** Cloud thickness is estimated as the difference between the retrieved cloud top and cloud base heights. It represents the thickness of the atmospheric layer where clouds were found to occur; although this approximation does not take into account the thickness of individual cloud layer forming under multilayer cloud conditions, it is easily reproducible and provides a sense of cloud thickness in this complex environment. Note that multilayer cloud conditions generally did not dominate the 1-hr period for which average cloud thickness is reported and as such are not expected to cause significant bias.

### 2.2.3. Precipitation Characteristics

In this study, we take the presence of a radar signal 90 m below any lidar-identified cloud base as an indication of the occurrence of precipitation. We make no distinction between precipitation types based on precipitation intensity (i.e., no distinction between drizzle and rain) and refer to all precipitation as rain. Given the sensitivity of the KAZR2 (approximately  $-45$  dBZ), we should expect to detect all rain falling at a rate above approximately  $2.9 \times 10^{-5} \text{ mm hr}^{-1}$  (Comstock et al., 2004).

- **Virga base height:** Below every detected liquid cloud base or melting layer (if any), the lowest height where a radar echo is observed is taken to be the base of the rain shaft (a.k.a. the virga base height). Note that since the KAZR2's lowest observation gate is located 60 m above the surface, reported virga base height might be underestimated (but by no more than 60 m) in cases where precipitation reaches the surface. Virga base height provides a measure of how close rain is to reaching the surface, something which may change in a changing climate and is of concerns to the surface hydrological cycle. Moreover, it provides information about the height at which evaporative cooling is expected to stop which influences mixing in the subcloud layer.
- **Surface precipitation flag:** Hours where at least two radar echoes are detected within 60 m from the surface are deemed to experience precipitation reaching the surface.
- **Rain-to-cloud fraction at the height below cloud base ( $\text{RCF}_{\text{CB}}$ ):** This quantity describes the percentage of the cloudy sky presenting rain at the height just below cloud base. It is estimated by dividing the number of columns with identified rain at the height just below cloud base within an hour by the number of



columns containing cloud at any height within an hour. Because rain was frequently observed to evaporate before reaching the surface, RCF at the height below cloud base is not necessarily equal to RCF near the surface; in fact, RCF was almost always observed to decrease with height. For the remainder of the analysis, we focus on characterizing RCF specifically at the height just below cloud base.

For rain rate quantification, we follow the technique described in Lamer et al. (2019) by which the combination of calibrated lidar and radar observations enables the detection of rain with mean diameter between 10 and 100  $\mu\text{m}$ . Since rain events above this intensity are also known to occur at the ENA observatory, gaps in the rain rate retrieval are filled using the Comstock et al. (2004) retrieval, which converts radar reflectivity ( $Z$  in  $\text{mm}^6 \text{m}^{-3}$ ) to rain rate ( $RR$  in  $\text{mm hr}^{-1}$ ) using  $Z = \alpha RR^\beta$  with  $\alpha = 25$  and  $\beta = 1.3$ . Note that the Comstock et al. (2004) retrieval is only applied to fill gaps where radar reflectivity is larger than 0 dBZ, thus ensuring that radar reflectivity is dominated by rain with minimum contribution from cloud droplets. The combined retrieval is expected to capture rain rates of all intensity above  $10^{-3} \text{ mm hr}^{-1}$ . Note that this rain rate quantification retrieval is less sensitive than the rain boundary retrievals described in the previous paragraphs.

- In-rain rain rate below formation level (in-rain  $RR_{CB}$ ): Here, we focus on reporting rain rate 90 m below its formation level defined here as cloud base or the melting layer height (if any). To make our rain rate estimate independent of precipitation area coverage, we report the average rain rate of only the precipitating portions of the hour (i.e., “in-rain” and not “whole-sky” nor “grid-box” average).

### 2.3. Observations and Estimation of Large-Scale Environmental Drivers

Motivated by Naud et al. (2018) findings that, in subsidence regimes, some parameters used to characterize the large-scale environment correlate well with cloud macrophysical characteristics, we tested whether these parameters can explain some of the variance in observed rain characteristics. The focus here is on parameters related to surface forcing and boundary layer stability, which we estimate as in Naud et al. (2018):

- Sea-air temperature contrast: skin temperature from the  $0.5^\circ \times 0.625^\circ$  spatial resolution MERRA-2 2017 1-hourly, time-averaged, single-level, assimilation reanalysis product (M2T1NXSLV V5.12.4) minus surface air temperature from the ARM meteorological station.
- Surface horizontal wind speed: measured by the ARM surface meteorological station.
- Surface relative humidity: measured by the ARM surface meteorological station.
- Estimated inversion strength (EIS) (Wood & Bretherton, 2006):  $EIS = \theta_{700} - \theta_{sf} - \Gamma_m^{850} (Z_{700} - LCL)$ , where  $\theta_{700}$  is the potential temperature at 700 hPa,  $\theta_{sf}$  the potential temperature of the air at the surface,  $\Gamma_m^{850}$  the lapse rate,  $Z_{700}$  the height of the 700 hPa isopressure level, and LCL the height of the lifting condensation level. All estimated using a combination of radiosonde and surface meteorological station measurements (see Naud et al., 2018, for details). In a nutshell, EIS is a measure of inversion strength where greater EIS is indicative of a stronger inversion; stronger inversions generally cause reduced dry air entrainment and thus allow for more effective trapping of moisture within the marine boundary layer, which is conducive to greater cloud cover.
- The Marine Cold Air Outbreak parameter (M parameter; Fletcher et al., 2016): skin potential temperature from the  $0.5^\circ \times 0.625^\circ$  spatial resolution MERRA-2 1-hourly, time-averaged, single-level, assimilation product (M2T1NXSLV V5.12.4) minus 800 hPa potential temperature obtained from radiosonde. In a nutshell, the M parameter is a measure of the absolute stability of the layer between 800 hPa and the surface. When the M parameter is positive, a cold air mass above a relatively warmer surface causes the boundary layer to be absolutely unstable. This tends to favor the organization of cellular convection, the typical signature of cold air outbreaks.

### 2.4. Correlation Between Properties and Drivers

In order to establish what conditions drive the character of rain, we perform several statistical correlative analyses. Specifically, we estimate the correlation between (1) cloud drivers and rain properties (results presented in section 3.2; Figure 3), (2) large-scale drivers and cloud properties (results presented in section 3.3; Figure 4), and finally (3) large-scale drivers and rain properties (results presented in section 3.4; Figures 7 and 8).

**Table 1**

Sample Size and Precipitation Characteristics for the Winter (DJF), Spring (MAM), Summer (JJA), and Fall (SON) Seasons for Postcold Frontal (PCF) and Non-PCF Subsidence Conditions

	DJF		MAM		JJA		SON		Total
	PCF	Non-PCF	PCF	Non-PCF	PCF	Non-PCF	PCF	Non-PCF	All <sub>sub</sub>
Cloud observation sample size (hrs)	159	998	269	1,502	333	1,926	118	1,994	7,299
Rain observation sample size (hrs)	151	850	263	1,158	294	1,360	90	1,703	5,869
Large-scale obs. sample size (hrs)	19	94	26	130	33	159	8	161	630
Subsidence periods with rain (%)	95	85	98	77	88	70	76	85	80
Periods with rain reaching the sfc. (%)	67	68	71	75	79	85	44	68	74
Periods w/rain and a melt. layer (%)	9	14	21	18	0	1	4	4	8
Melting height (km)									
Median	1.0	[, ]1.1 [1.0, 1.5]	1.2	[, ]1.2 [1.0, 1.5]	—	3.0 [2.9, 3.6]	1.5	1.7 [1.5, 2.6]	1.2
[25th, 75th] percentiles	[0.9, 1.1]		[1.0, 1.6]				[1.5, 1.6]		[1.0, 1.7]

To maintain a large enough sample size, we perform these correlative analyses using the entire pool of subsidence observations including PCF and non-PCF periods of all seasons. Insight into the statistical relationship between precipitation and cloud attributes and driver intensity is gained by organizing our samples based on the intensity of each driver; here, in each of the aforementioned figures, the distribution of rain properties in each driver intensity bin is depicted by the shaded background. This distribution is scaled by the total number of available observations and as such represents the percentage of all observations falling into each rain property and large-scale driver intensity interval (referred to as observation density). Then, for each driver intensity interval (i.e., bin), we estimate the median of all observed precipitation or cloud characteristics. This procedure produces relations between binned driver intensities and median precipitation or cloud properties. We assess how well this median relationship between the two variables can be described using a monotonic—but not necessarily linear—function through the estimation of their Spearman correlation coefficient ( $R$ ). Here, in each of the aforementioned figures, the median relationship is depicted by either a solid or dashed line depending on whether or not it is statistically significant at  $p < 0.05$ . In some instances, median relationships are also estimated for subsets of the observational data set (e.g., without melting layer or cloud base height between 0.8–1.5 km) in which case only the median relationship is depicted and not the distribution of rain properties in each driver intensity bin specific to the subset.

Consistency is used when constructing the driver intensity bins. The range—from the 5th to the 95th percentile—of observed values for each driver is split to yield 12 evenly distributed driver intensity bins. In the few bins that do not contain at least 3% of all available observations, the median cloud or precipitation characteristics is not estimated. Resulting bin size for sea-air temperature contrast is 0.35 K, for surface horizontal wind speed  $0.76 \text{ m s}^{-1}$ , for surface relative humidity 2.89%, for EIS 0.80 K, for the M parameter 1.19 K, and for cloud thickness 61.43 m.

## 2.5. Data Availability

For the period between October 2015 and September 2018, the ARM ground-based remote sensors collected over 7,000 hrs of cloud observations during subsidence conditions; precipitation was detected during 80% of these hours and 8% of the precipitating hours presented a melting layer. For the characterization of the large-scale environment, over 630 balloon-borne radiosondes were launched during these precipitating subsidence hours (Table 1; “Total” column). For reference, this data set overlaps with that of Naud et al. (2018) but excludes the period before the installation of the KAZR2, which is more sensitive to light precipitation than its predecessor the W-band ARM Cloud Radar (WACR). The current data set also includes the additional 9-month period between January 2018 and September 2018, which was not available at the time of the Naud et al. (2018) analysis.

For each of the seasons of winter (December–February, DJF), spring (March–May, MAM), summer (June–August, JJA), and fall (September–November, SON), more than 90 hrs of precipitation observations and 8 to 33 of the radiosondes launches were collected during PCF events (Table 1; Gray columns).

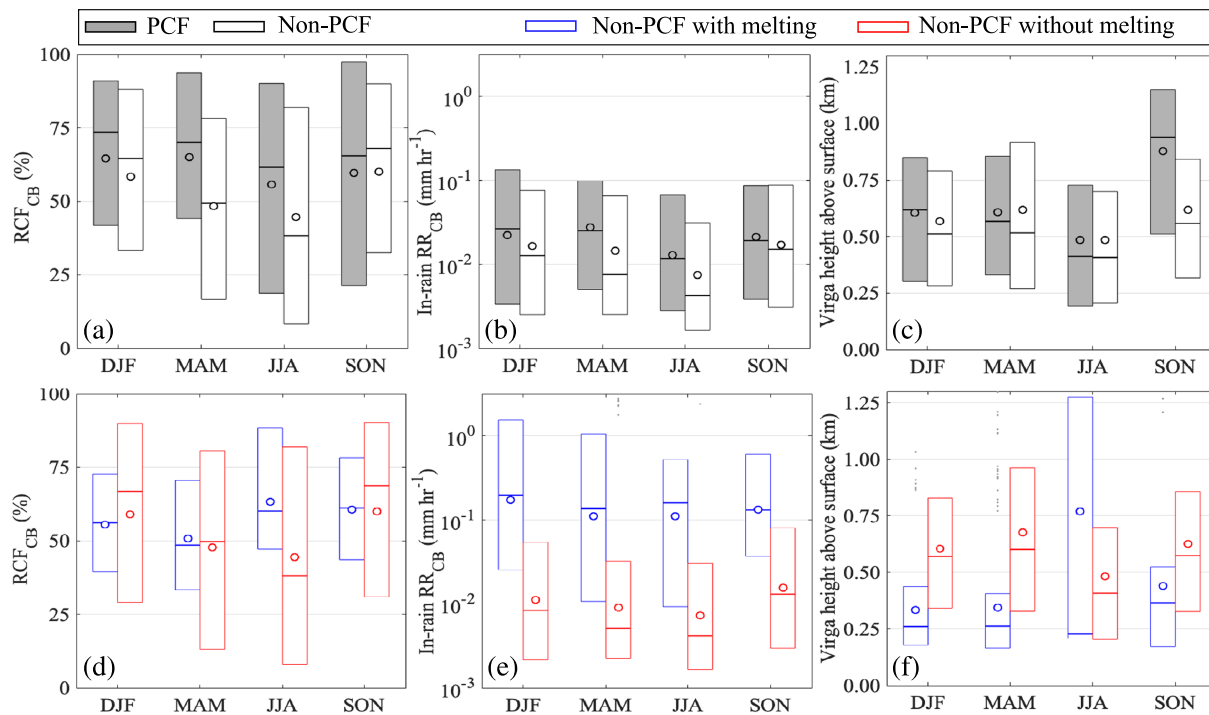


**Figure 2.** Seasonal cycle of (a and d) rain-to-cloud fraction at the level below cloud base, (b and e) in-rain rain rate at the level below cloud base, and (c and f) virga base height above the surface. Seasonal cycles are depicted for subsidence conditions post- cold frontal (PCF; gray boxes) and non-PCF (white boxes with black outline) as well as the subset of non-PCF conditions showing signs of melting (white box with blue outline) and not showing signs of melting (white box with red outline). Seasonal cycles cover the winter (DJF), spring (MAM), summer (JJA), and fall (SON) seasons. This figure depicts the seasonal mean (circle), median (center line), interquartile range (box), and outliers (dots). These results are also tabulated in Table S1.

### 3. Results

To provide a broad overview of the observational data set, we first present the seasonal characteristics of precipitation and especially how they differ following the passage of a cold front in contrast to general subsidence conditions (section 3.1). Then we examine how precipitation characteristics relate to cloud properties (section 3.2) and to large-scale characteristics (section 3.4).

#### 3.1. Rain Characteristics in the Wake of Cold Fronts

Analysis of the 3-year data set shows evidence that the seasonal cycle of precipitation specific to events following the passage of a cold front is different from that of precipitation forming under general subsidence conditions.

A number of differences between PCF and non-PCF conditions are found to persist from winter through summer (Table 1 and Figure 2, top panels). For instance, the propensity to precipitate of clouds forming in PCF subsidence periods is observed to be roughly 10% higher than that of clouds forming during general subsidence periods (Table 1). For those events producing rain, PCF events tend to be associated with slightly higher  $RCF_{CB}$  than non-PCF events. The largest difference between both regimes occurs in the summer where median  $RCF_{CB}$  is 62% in PCF events and only 38% in non-PCF events (Figure 2a). Higher rain intensity is observed at the base of clouds forming during PCF events (median  $RR_{CB} \sim 2.5 \times 10^{-2} \text{ mm hr}^{-1}$ ) in contrast to those formed in non-PCF events (median  $RR_{CB} \sim 1.2 \times 10^{-2} \text{ mm hr}^{-1}$ ; Figure 2b). However, PCF events are generally associated with rain evaporating several meters higher in the boundary layer (i.e., higher median virga base height; Figure 2c). Despite this, PCF and non-PCF events present a very similar fraction of events producing at least some precipitation reaching down to the surface within any 1-hr time period (e.g., 67% of observed PCF hours vs. 68% of observed non-PCF hours presented signs of surface rain in the winter; Table 1).

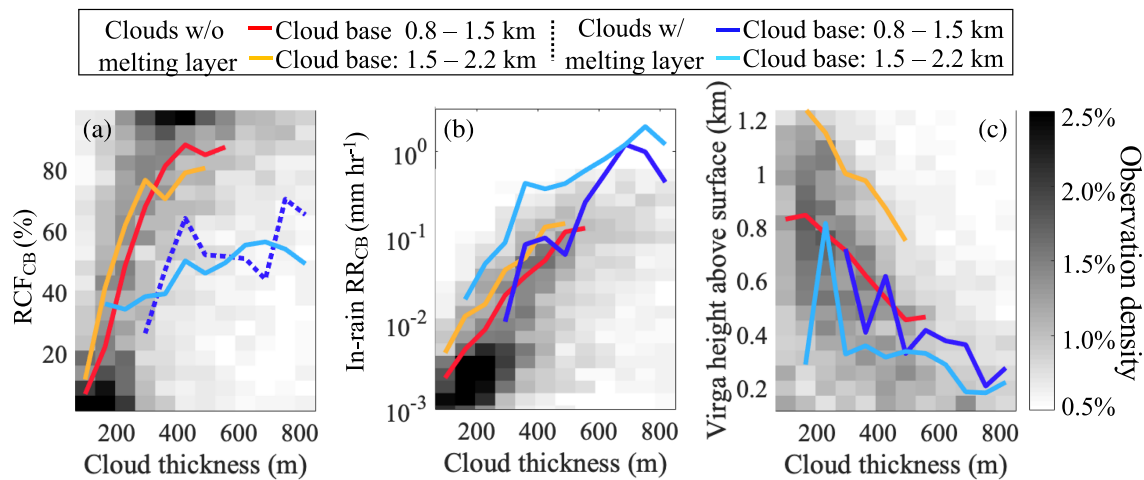


**Figure 3.** Relationship between (a) median rain-to-cloud fraction at the level below cloud base, (b) median in-rain rain rate at the level below cloud base or the melting layer height, and (c) median virga base height and cloud thickness. Relationships are estimated using subsets of PCF and non-PCF periods: purely liquid clouds with cloud base between 0.8 and 1.5 km (red) or cloud base between 1.5 and 2.2 km (yellow) and cloud with melting layer and cloud base between 0.8 and 1.5 km (royal blue) or cloud base between 1.5 and 2.2 km (light blue). Relationships with a Spearman correlation coefficient ( $R$ ) significant at  $p < 0.05$  are plotted as solid and not significant as dashed. Black shading represents the distribution of rain properties in each cloud thickness bin for the entire data set, which comprises the subsets for which the median relationships are estimated.

The aforementioned relationships are observed to change in the fall season. In the fall season, rather than showing an enhanced propensity to precipitate in contrast to non-PCF, PCF conditions exhibit a 10% lower fraction of events with precipitation. Also, only in the fall season do PCF and non-PCF conditions experience nearly the same seasonal median RCF<sub>CB</sub>. Finally, although seasonal median in-rain RR<sub>CB</sub> remains close to the yearly average and is similar for PCF and non-PCF conditions, in the fall median virga base height is the most elevated among all seasons (940 m for PCF and 558 m for non-PCF).

Evidence of the presence of melting layers around 1.2 km altitude (Table 1) suggests that although all precipitation reaching the surface under subsidence conditions is of liquid phase, some of this rain was initially produced through ice microphysical processes. PCF and non-PCF events roughly have the same fraction of rain events exhibiting melting layer (e.g., 9% for PCF relative to 14% for non-PCF in the winter and 21% for PCF and 18% for non-PCF in the spring), suggesting that cold front passages do not systematically promote the formation of ice-topped boundary layer clouds. Note that the fraction of events associated with melting is largest in the spring and smallest in the summer in both PCF and non-PCF events (Table 1). Because the non-PCF data set has the largest sample size, we use it to examine the differences in rain characteristics resulting from these melt events (Figure 2, bottom panels). Events originating from the melting of ice crystals have a seasonal median RCF<sub>CB</sub> similar to liquid-topped cloud events (Figure 2d), but more intense rain (Figure 2e) generally penetrating further downward (Figure 2f).

### 3.2. Relationship Between Cloud Macrophysics and Rain in Complex Cloud Systems

In an effort to explain the differences in precipitation properties observed during PCF and non-PCF conditions, we investigate what controls precipitation properties. Prior studies have found evidence that cloud thickness has a large impact on rain occurrence, RCF, virga depth, and rain rate in stratiform boundary layer clouds. These studies however relied on a set of assumptions, for example, one relied on cloud top height as a proxy for cloud thickness (Kubar et al., 2009), or heavily constrained their data sets (Yang et al., 2018). Therefore, it is unclear whether these relationships are applicable to all shallow cloud conditions occurring in the ENA region: a region where it is not uncommon to see, within the course of only a few days, single-layer stratocumulus decks transitioning into complex systems exhibiting break ups, shallow cumulus with stratiform outflows, and sometimes containing a melting layer (e.g., Figure 1). Other examples of such cases are presented in Miller and Albrecht (1995) and Miller et al. (1998).

Analysis of our 3-year data set indicates that cloud thickness does relate to precipitation properties even in the often-complex cloud situations that are found in the ENA region. To be exact, the relationships created



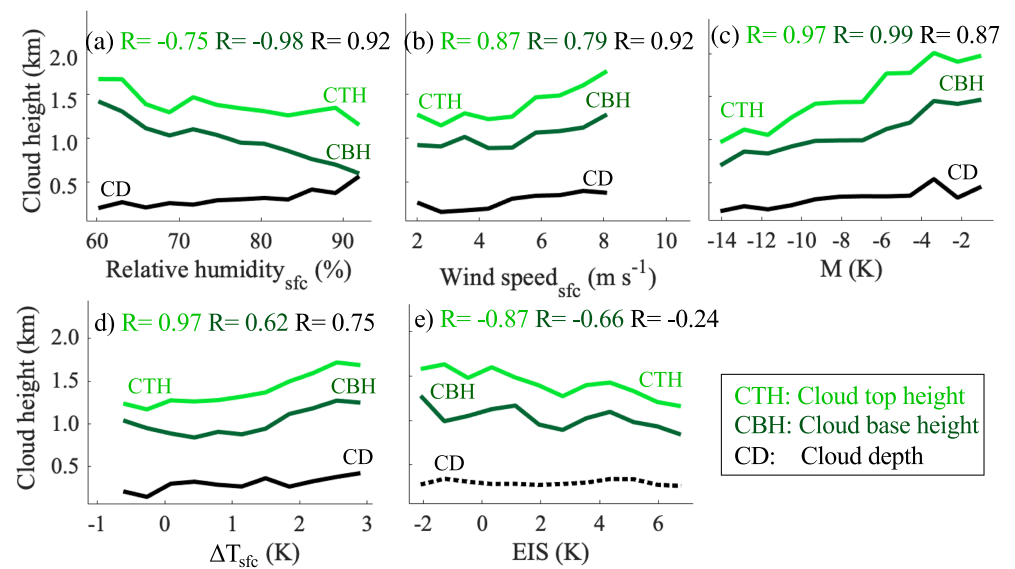


**Figure 4.** Relationships between median cloud top height (light green), median cloud base height (forest green), and median cloud depth (black) and various large-scale drivers. Relationships are estimated using all observed subsidence conditions (both PCF and non-PCF). The large-scale drivers plotted include (a) surface relative humidity, (b) surface horizontal wind speed, (c) the M parameter, (d) sea air temperature contrast, and (e) estimated inversion strength. Relationships with a Spearman correlation coefficient ( $R$ ) significant at  $p < 0.05$  are plotted as solid and not significant as dashed.

by estimating median  $RCF_{CB}$  (Figure 3a), median in-rain  $RR_{CB}$  (Figure 3b), and median virga base height (Figure 3c) for various cloud thickness intervals were found to be statistically significant when considering all subsidence conditions observed (median relationships not shown; however, black shading represents the distribution of rain properties in each cloud thickness bin used to derive the median relationships). Higher statistical significance was achieved when estimating relationships for the subsets of purely liquid cloud or clouds with melting forming at different height: specifically, purely liquid clouds with cloud base between 0.8 and 1.5 km (red) or cloud base between 1.5 and 2.2 km (yellow) and cloud with melting layer and cloud base between 0.8 and 1.5 km (royal blue) or cloud base between 1.5 and 2.2 km (light blue; Figure 3).

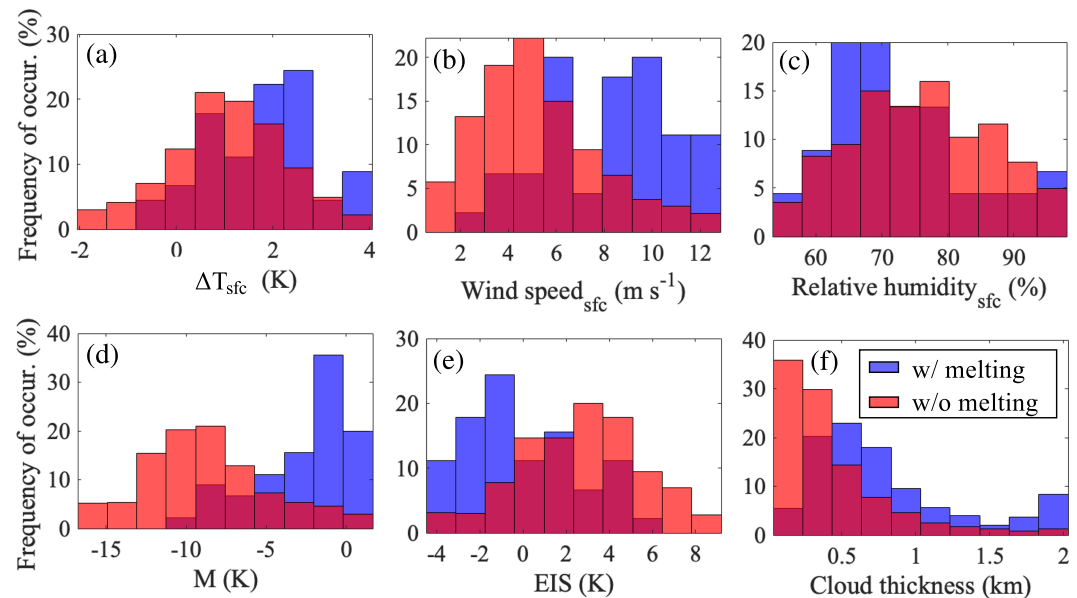
Generally speaking, these relationships show that for larger cloud thickness,  $RCF_{CB}$  is larger, in-rain  $RR_{CB}$  is higher, and rain shafts reach closer to the surface (i.e., lower virga base height). Specifics of the relationship between cloud thickness and  $RCF_{CB}$  depend on the microphysical regime under which rain was formed: For clouds of similar thickness and cloud base height, melting conditions are associated with smaller  $RCF$  at the level 90 m below cloud base. However, the effect of melting on rain rate below its formation level (cloud base or the melting layer; Figure 3b) and virga base height (Figure 3c) is not as clear. It is important to recall that cloud thickness and cloud base height are here defined in terms of the height of the lowest liquid layer, which for melting conditions may be different from the base of the ice/mixed phase cloud.

Figure 3c also reveals that, for liquid-topped clouds, the lowest height reached by precipitation also strongly depends on cloud base height which is expected given that it controls the path length precipitation must fall through before reaching the surface. Also, more elevated clouds are likely associated with slightly higher in-rain  $RR_{CB}$  (Figure 3b red vs. yellow line).

Although cloud thickness and cloud base height appear to be good predictors of precipitation properties, they may not be the only factors influencing its character especially knowing how sensitive clouds forming in subsidence regimes are to their environment (Naud et al., 2018).

### 3.3. Impact of Large-Scale Conditions on Cloudiness

Analysis performed by Naud et al. (2018) indicates that differences in cloud attributes observed between PCF and non-PCF conditions could be explained by their differences in large-scale conditions, implying that



**Figure 5.** (a) Sea-air temperature contrast, (b) surface horizontal wind speed, (c) surface relative humidity, (d) the M parameter, (e) estimated inversion strength, and (f) cloud thickness observed during ice-topped (blue bars) and liquid-topped (red bars) events both PCF and non-PCF. Dark red bars are visible where both bar graphs overlap.

large-scale conditions can be a driver of cloud variability. Revisiting Naud et al. (2018)'s work using our data set (see section 2.5 for details on both data sets), we come to similar conclusions: The large-scale parameters most strongly related to cloud thickness include (in order of strongest correlation) surface relative humidity (Figure 4a), surface horizontal wind speed (Figure 4b), the Marine Cold Air Outbreak M parameter (Figure 4c), and the sea-air temperature contrast (Figure 4d). All these parameters are also found to have an effect on cloud base and cloud top height, suggesting that beyond leading to a thickening of the cloud deck, these large-scale parameters impact the vertical location of the cloud deck. In other words, more unstable conditions (higher M parameter) and greater surface forcing (higher horizontal wind speed and higher sea-air temperature contrast) coincide with more elevated and deeper cloud layers (Figure 4). In addition to the aforementioned large-scale parameters, changes in EIS are also found to be associated with changes in the cloud deck height—but not the cloud deck thickness (Figure 4e). Finally speaking to factors influencing cloud microphysical phase, the largest distinction between melt and melt-free regimes was found to be in the distributions of their M parameter (Figure 5d) and to some extent of their horizontal wind speed (Figure 5b): both higher for melt conditions. This difference stands out especially given the similarities in their distribution of sea-air temperature contrast and relative humidity (Figures 5a and 5c).

Given the strong tie between cloud and precipitation, we hypothesize that large-scale parameters also have an impact on precipitation.

### 3.4. Impact of Large-Scale Conditions on Rain

Similarities in the seasonal cycle of rain properties (Figure 2) and large-scale conditions (Figure 6) under both PCF and non-PCF conditions further support the idea that large-scale conditions might influence the character of precipitation.

For example, the seasonal pattern of median virga base height (Figure 2c) seems to mirror that of the median surface relative humidity (Figure 6c) and median M parameter (Figure 6d) where seasonal extremes in median values specific to both PCF and non-PCF conditions, as well as the largest differences between median values for PCF and non-PCF conditions occur in the fall. Pooling all subsidence periods regardless of their season, we find that there is indeed a statistically significant monotonic relationship between surface relative humidity and median virga base height where increases in surface relative humidity are associated with precipitation events reaching closer to the surface ( $R_{\text{all}} = -0.94$ ; Figure 7a, black color). An explanation for this

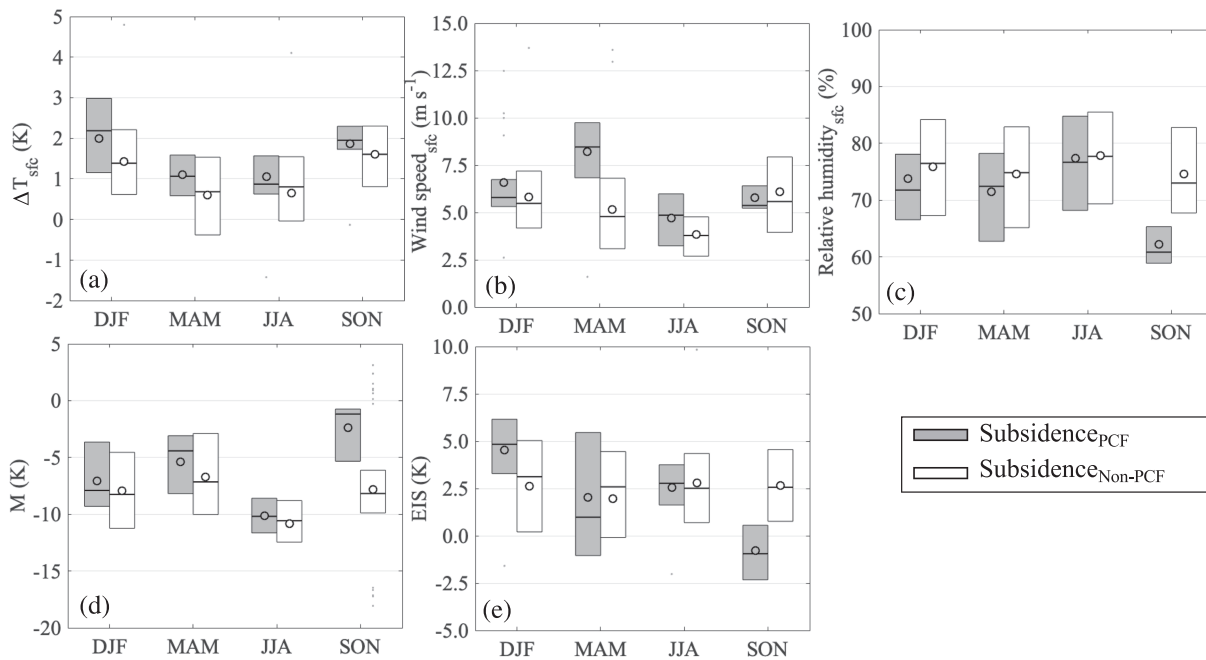


**Figure 6.** Seasonal cycle of (a) sea-air temperature contrast, (b) surface horizontal wind speed, (c) surface relative humidity, (d) the M parameter, and (e) estimated inversion strength under subsidence conditions postcold frontal (PCF; gray boxes) and non-PCF (white boxes). Seasonal cycle covers the winter (DJF), spring (MAM), summer (JJA), and fall (SON) seasons. This figure depicts the seasonal mean (circle), median (center line), interquartile range (box), and outliers (dots). Results are also tabulated in Table S2.

could be that drop evaporation rates both decrease with increasing relative humidity and lead to an increase in relative humidity. The M parameter also relates to median virga base height, indicating that boundary layer stability also plays a role in determining how close to the surface rain will reach before totally evaporating (Figure 7b). Under the range of M parameter conditions associated with liquid-topped cloud conditions (M parameter < −4 K), increases in the M parameter (i.e., more instability) are found to be associated with significantly more elevated rain ( $R_{w/o \text{ melt}} = 0.76$ ; Figure 7b red color). Conversely, under

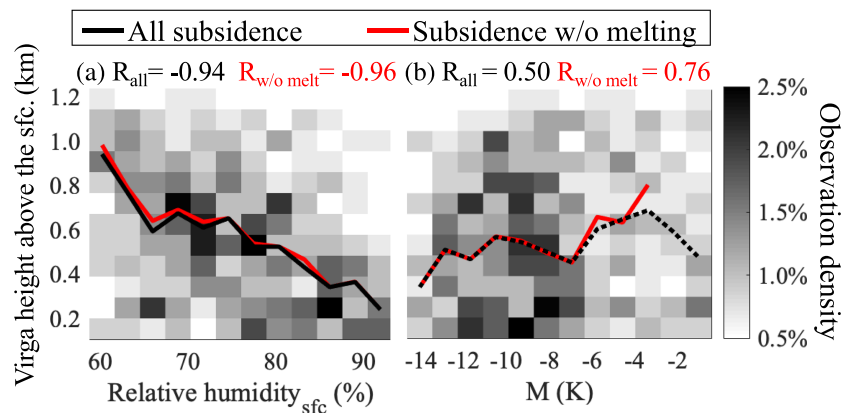


**Figure 7.** Relationships between median virga base height and (a) surface relative humidity and (b) the M parameter for all observed subsidence conditions (both PCF and non-PCF; black lines, “all subsidence”) and for the subset of cases strictly without a melting layer (red lines, “subsidence w/o melting”). Relationships with a Spearman correlation coefficient ( $R$ ) significant at  $p < 0.05$  are plotted as solid and not significant as dashed. Black shading represents the distribution of rain properties in each large-scale driver intensity bin used to estimate the median specific to the “all subsidence” conditions category; the distribution of rain properties in each large-scale driver intensity bin specific to the “subsidence w/o melting” subset is not shown.

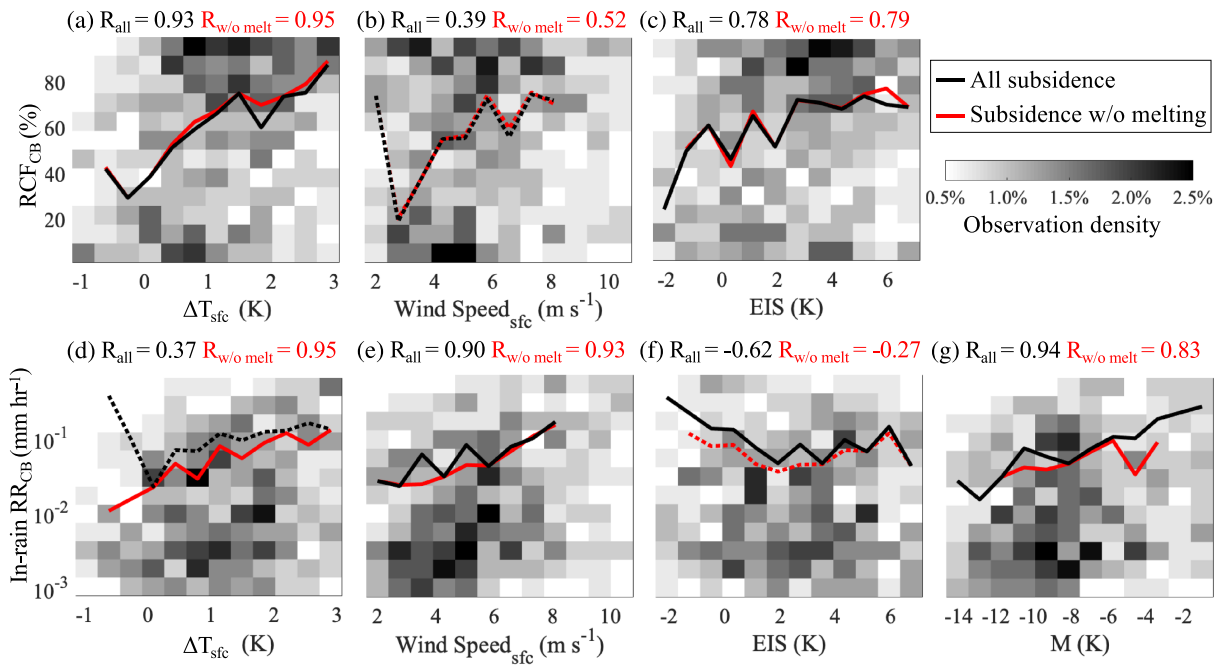


**Figure 8.** Relationships between median rain-to-cloud fraction at the level below cloud base and (a) sea air temperature contrast, (b) surface horizontal wind speed, and (c) estimated inversion strength for all observed subsidence conditions (both PCF and non-PCF; black lines, “all subsidence”) and for the subset of cases strictly without a melting layer (red lines, “subsidence w/o melting”). Also plotted are the relationships between median in-rain rain rate at the level below cloud base and (d) sea air temperature contrast, (e) surface horizontal wind speed, (f) estimated inversion strength, and (g) the M parameter. Relationships with a Spearman correlation coefficient ( $R$ ) significant at  $p < 0.05$  are plotted as solid and not significant as dashed. Black shading represents the distribution of rain properties in each large-scale driver intensity bin used to estimate the median specific to the “all subsidence” conditions category; the distribution of rain properties in each large-scale driver intensity bin specific to the “subsidence w/o melting” subset is not shown.

relatively more unstable conditions ( $M$  parameter  $> -4$  K), increasingly unstable conditions are associated with rain reaching closer to the surface (i.e., lower virga base height; Figure 7b, black color). This seems to indicate that rain responds differently to the large scale under highly unstable conditions, which coincidentally are also observed to more frequently be associated with melt events (Figure 5).

Unlike virga base height, the seasonal cycle of  $RCF_{CB}$  (Figure 2a) does not share the same similarities with any one large-scale drivers under both PCF and non-PCF conditions (Figure 6). Under PCF conditions, the seasonal cycle of  $RCF_{CB}$  seems to best mirror that of surface horizontal wind speed (Figure 6b), while under non-PCF conditions, it seems to best mirror the cycle of sea-air temperature contrast (Figure 6a). Correlative studies indicate that median  $RCF_{CB}$  is statistically significantly related to both the sea-air temperature contrast ( $R_{all} = 0.93$ ; Figure 8a, black color) and the EIS ( $R_{all} = 0.78$ ; Figure 8c, black color). Surface horizontal wind speed also shows a relationship with median  $RCF_{CB}$ , one that is more significant for liquid-topped conditions ( $R_{w/o\ melt} = 0.52$ ; Figure 8b, red color). So both surface forcing and boundary layer stability parameters show a link with RCF at the level below cloud base.

While patterns in the seasonal cycle of in-rain rain rate at the level below cloud base (in-rain  $RR_{CB}$ ; Figure 2b) do not provide indications as to its connection to any large-scale parameter, pooling all hourly subsidence conditions reveals that the median in-rain  $RR_{CB}$  is most strongly related to surface horizontal wind speed ( $R_{all} = 0.90$ ; Figure 8e black color) and the  $M$  parameter ( $R_{all} = 0.94$ ; Figure 8g, black color). Also, similarly to  $RCF_{CB}$ , median in-rain  $RR_{CB}$  is also found to be related to the sea-air temperature contrast. That being said, the relationship between in-rain  $RR_{CB}$  and the sea-air temperature contrast is found to be monotonic under liquid-topped cloud conditions ( $R_{w/o\ melt} = 0.95$ ; Figure 8d red color) but not significant when considering melt events especially under warm air advection scenario (Figure 8d, black color, region with  $\Delta T_{sfc} < 0$  K) hinting to the fact that microphysics also influence in-rain  $RR_{CB}$ . Taken together this suggests that rain rate near cloud base level is influenced by surface forcing (including heat fluxes), boundary layer stability, and microphysics.



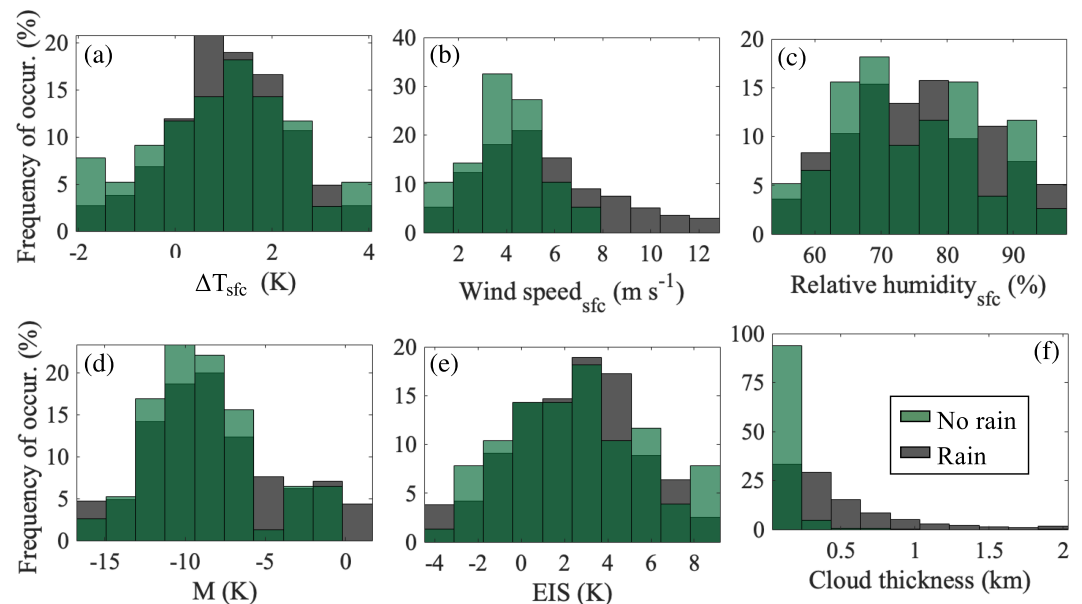


**Figure 9.** (a) Sea-air temperature contrast, (b) surface horizontal wind speed, (c) surface relative humidity, (d) the M parameter, (e) estimated inversion strength, and (f) cloud thickness observed during precipitating (light green bars) and nonprecipitating (gray bars) subsidence periods both PCF and non-PCF. Dark green bars are visible where both bar graphs overlap.

The current work highlights that more than one driver influences each of the aforementioned precipitation properties. Analysis of the slope of each relationship, which have been estimated across the same range of observed values (5th to 95th percentile), provides preliminary evidence of the relative importance of each driver. Note however that given the nonlinearity of some of these relationships, the driver most influential on a certain precipitation property may change based on the large-scale regime in which rain formed. For example, the same variation in horizontal wind speed would lead to larger changes in  $RCF_{CB}$  in a “low” wind-speed regime in contrast to in a “high” wind-speed regime (see Figure 8b).

Finally, seeking to determine what controls a cloud’s propensity to precipitate (related to precipitation onset), we compare the large-scale and cloud properties associated with nonprecipitating events and precipitating events. Figure 9 supports a previous hypothesis that cloud thickness is a limiting factor to rain formation (Kubar et al., 2009) and suggests that large-scale conditions are not. Figure 9b also shows that rain was systematically observed during periods with wind speeds exceeding  $8 \text{ m s}^{-1}$ , which could indicate that conditions with higher horizontal wind speeds are more conducive to rain formation. Further interpretation of Figure 9 is complicated by the fact that the current results are based on point observations and as such cannot capture the complete life cycle of individual clouds.

#### 4. Conclusions

Using a combination of reanalysis and observations collected over 3 years at the Atmospheric Radiation Measurement (ARM) program Eastern North Atlantic (ENA) observatory, we characterize the precipitation and cloud properties occurring during general subsidence conditions as well as those specifically resulting from the passage of a cold front.

Observations show that Post-Cold Frontal (PCF) subsidence periods have seasonal variations in cloud propensity to precipitate, Rain-to-Cloud Fraction at the level below cloud base ( $RCF_{CB}$ ), and virga base height different from general subsidence periods (non-PCF). This suggests that cold front passages affect the character of precipitation occurring in the low-level clouds forming in their wake.

Some of these differences can be explained by the fact that the macrophysical properties of the clouds forming in these regimes strongly correlates with these rain properties:

- i Deeper clouds are generally associated with higher  $RCF_{CB}$  and rain rate at the level below cloud base ( $RR_{CB}$ ) and to rain reaching closer to the surface and,
- ii higher cloud bases are generally associated with more elevated virga.

These results, obtained with observations of a wide range of shallow cloud types from well-researched single-layer stratocumulus to more complex cumulus-stratocumulus fields, demonstrate the robustness of these previously documented relationships between cloud thickness and rain characteristics. Our results also suggest that these relationships hold when rain results from snow melting although for the same thickness, ice-topped clouds were associated with lower  $RCF_{CB}$  than liquid-topped clouds. The seasonal cycle of cloud boundaries specific to the conditions discussed here are illustrated in Figure S1 in the supporting information for reference.

Of broader interest here is identifying other factors that could drive precipitation variability, which may also further help explain the differences in precipitation characteristics observed between PCF and non-PCF subsidence conditions. Monotonic relationships are identified between a number of large-scale parameters and rain properties:

- i Higher sea-air temperature contrast and higher surface horizontal wind speed are both associated with higher  $RCF_{CB}$  and ( $RR_{CB}$ ),
- ii higher EIS is found to relate to higher  $RCF_{CB}$  (as speculated by Kubar et al., 2009) and,
- iii higher Estimated Inversion Strength (EIS) is also to some extent found to relate to lower  $RR_{CB}$  (in general agreement with Wu et al., 2017), although higher M parameter (also a measure of atmospheric stability) was found to have a much more consistent relationship. Lower correlations between both cloud and rain properties with EIS perhaps relate to the fact that some of the observed clouds are advected rather than locally formed. Advected clouds take more time to respond to local processes related to changes in inversion strength (i.e., vertical entrainment mixing) than to other properties (e.g., relative humidity).
- iv We also identify the parameter M and relative humidity to be highly related to the virga base height.

While statistically significant, the aforementioned relationships based on median rain properties estimated within intervals of large-scale driver intensity do not perfectly represent all observed conditions as depicted by the background shading in Figures 7 and 8. Also note that there is more scatter in the precipitation properties observed in each large-scale driver intensity bin than there is in each cloud thickness bin (contrasting Figures 7–8 and Figure 3, respectively). We note that some of the increase in scatter could result from large-scale and rain properties having been sampled using different sensors and to the smaller sample size of the large-scale properties relative to the cloud properties (see Table 1,  $All_{sub}$  for sample sizes). However, this larger variability and the existence of relationships between large-scale conditions and cloud could also suggest that the large-scale has an indirect effect on determining the character of precipitation through its control on cloud macrophysics.

Isolating liquid-topped events from those exhibiting melting mostly increased the strength of these correlations. While the size of our large-scale data set with melting is limited (~50 hrs), this result suggests that the microphysical processes associated with melting alter the relationships between the large-scale environment and rain. Despite the small sample size, it is evident that elevated M parameter (i.e., more unstable conditions) and higher horizontal wind speed are observed conjointly with melting. Additional statistics on the large-scale conditions associated with non-PCF conditions presenting melting are given in Figure S2 for reference.

Overall, this study provides new sets of observational benchmarks for evaluating the properties of numerically modeled rain in subsidence conditions, especially following the passage of a cold front. Our characterization of the connections between rain and cloud in complex shallow cloud systems both liquid- and ice-topped offers opportunities to refine and/or develop new parametrizations. Additional insight could also be gained from exploring the relationships between the various rain properties characterized in the current study, such as the connection between rain rate and virga base height and/or by considering the influence of decoupling or mesoscale cellular convection patterns on rain properties. Here, our additional finding that several large-scale properties significantly correlate with rain attributes suggests that a realistic representation of rain properties in models relies on the accurate representation of both clouds and the large-scale environment.

## Acknowledgments

The contributions of all three authors were funded by the U.S. Department of Energy office of science Grant DE-SC0016344 as part of the Atmospheric Systems Research (ASR) program. The MERRA-2 files were obtained from the NASA Goddard Earth Sciences Data and Information Services Center at <https://disc.sci.gsfc.nasa.gov/>. The MCMS data set was obtained from the GWEX Cloud System Study repository at <https://gcss-dime.giss.nasa.gov/mcms/>. All observations were obtained from the ARM archive at <https://www.archive.arm.gov/discovery/>, which also hosts the retrievals of rain rates and cloud microphysical phase at <https://arm.gov/data/data-sources/precipmicrophys-kazlidar-158>.

## References

- Ahlgrimm, M., & Forbes, R. (2014). Improving the representation of low clouds and drizzle in the ECMWF model based on ARM observations from the Azores. *Monthly Weather Review*, 142(2), 668–685.
- Bauer, M., & Del Genio, A. D. (2006). Composite analysis of winter cyclones in a GCM: Influence on climatological humidity. *Journal of Climate*, 19(9), 1652–1672.
- Bodas-Salcedo, A., Williams, K., Field, P., & Lock, A. (2012). The surface downwelling solar radiation surplus over the Southern Ocean in the Met Office model: The role of midlatitude cyclone clouds. *Journal of Climate*, 25(21), 7467–7486. <https://doi.org/10.1175/JCLI-D-11-00702.1>
- Bodas-Salcedo, A., Williams, K. D., Ringer, M. A., Beau, I., Cole, J. N., Dufresne, J.-L., et al. (2014). Origins of the solar radiation biases over the Southern Ocean in CFMIP2 models. *Journal of Climate*, 27(1), 41–56. <https://doi.org/10.1175/JCLI-D-13-00169.1>
- Comstock, K. K., Wood, R., Yuter, S. E., & Bretherton, C. S. (2004). Reflectivity and rain rate in and below drizzling stratocumulus. *Quarterly Journal of the Royal Meteorological Society*, 130(603), 2891–2918.
- Fletcher, J., Mason, S., & Jakob, C. (2016). The climatology, meteorology, and boundary layer structure of marine cold air outbreaks in both hemispheres. *Journal of Climate*, 29(6), 1999–2014.
- Gelaro, R., McCarty, W., Suárez, M. J., Todling, R., Molod, A., Takacs, L., et al. (2017). The modern-era retrospective analysis for research and applications, version 2 (MERRA-2). *Journal of Climate*, 30(14), 5419–5454.
- Gettelman, A., & Morrison, H. (2015). Advanced two-moment bulk microphysics for global models. Part I: Off-line tests and comparison with other schemes. *Journal of Climate*, 28(3), 1268–1287. <https://doi.org/10.1175/JCLI-D-14-00102.1>
- Kay, J. E., L'Ecuyer, T., Pendergrass, A., Chepfer, H., Guzman, R., & Yettella, V. (2018). Scale-aware and definition-aware evaluation of modeled near-surface precipitation frequency using CloudSat observations. *Journal of Geophysical Research: Atmospheres*, 123(8), 4294–4309.
- Kollias, P., Puigdomènech Treserras, B., & Protat, A. (2019). Calibration of the 2007–2017 record of Atmospheric Radiation Measurements cloud radar observations using CloudSat. *Atmospheric Measurement Techniques*, 12(9), 4949–4964.
- Kubar, T. L., Hartmann, D. L., & Wood, R. (2009). Understanding the importance of microphysics and macrophysics for warm rain in marine low clouds. Part I: Satellite observations. *Journal of the Atmospheric Sciences*, 66(10), 2953–2972.
- Lamer, K., Puigdomènech Treserras, B., Zhu, Z., Isom, B., Bharadwaj, N., & Kollias, P. (2019). Characterization of shallow oceanic precipitation using profiling and scanning radar observations at the Eastern North Atlantic ARM observatory. *Atmospheric Measurement Techniques*, 12(9), 4931–4947. <https://doi.org/10.5194/amt-12-4931-2019>
- Lau, N.-C., & Crane, M. W. (1997). Comparing satellite and surface observations of cloud patterns in synoptic-scale circulation systems. *Monthly Weather Review*, 125(12), 3172–3189. [https://doi.org/10.1175/1520-0493\(1997\)125<3172:CSASOO>2.0.CO;2](https://doi.org/10.1175/1520-0493(1997)125<3172:CSASOO>2.0.CO;2)
- Leon, D. C., Wang, Z., & Liu, D. (2008). Climatology of drizzle in marine boundary layer clouds based on 1 year of data from CloudSat and Cloud-Aerosol Lidar and Infrared Pathfinder Satellite Observations (CALIPSO). *Journal of Geophysical Research*, 113, D00A14. <https://doi.org/10.1029/2008JD009835>
- Miller, M. A., & Albrecht, B. A. (1995). Surface-based observations of mesoscale cumulus–stratocumulus interaction during ASTEX. *Journal of the Atmospheric Sciences*, 52(16), 2809–2826.
- Miller, M. A., Jensen, M. P., & Clothiaux, E. E. (1998). Diurnal cloud and thermodynamic variations in the stratocumulus transition regime: A case study using in situ and remote sensors. *Journal of the Atmospheric Sciences*, 55(13), 2294–2310.
- Morrison, H., & Gettelman, A. (2008). A new two-moment bulk stratiform cloud microphysics scheme in the community atmosphere model, version 3 (CAM3). Part I: Description and numerical tests. *Journal of Climate*, 21(15), 3642–3659.
- Naud, C. M., Booth, J. F., & Genio, A. D. D. (2014). Evaluation of ERA-Interim and MERRA cloudiness in the Southern Ocean. *Journal of Climate*, 27(5), 2109–2124. <https://doi.org/10.1175/jcli-d-13-00432.1>
- Naud, C. M., Booth, J. F., & Lamraoui, F. (2018). Post cold frontal clouds at the ARM Eastern North Atlantic Site: An examination of the relationship between large-scale environment and low-level cloud properties. *Journal of Geophysical Research: Atmospheres*, 123, 12,117–12,132. <https://doi.org/10.1029/2018JD029015>
- Naud, C. M., Jeyaratnam, J., Booth, J. F., Zhao, M., & Gettelman, A. (2020). Evaluation of modeled precipitation in oceanic extratropical cyclones using IMERG. *Journal of Climate*, 33(1), 95–113.
- Paluch, I., & Lenschow, D. (1991). Stratiform cloud formation in the marine boundary layer. *Journal of the Atmospheric Sciences*, 48(19), 2141–2158.
- Rémillard, J., Kollias, P., Luke, E., & Wood, R. (2012). Marine boundary layer cloud observations in the Azores. *Journal of Climate*, 25(21), 7381–7398.
- Rémillard, J., & Tselioudis, G. (2015). Cloud regime variability over the Azores and its application to climate model evaluation. *Journal of Climate*, 28(24), 9707–9720.
- Rotsteyn, L. D. (1997). A physically based scheme for the treatment of stratiform clouds and precipitation in large-scale models. I: Description and evaluation of the microphysical processes. *Quarterly Journal of the Royal Meteorological Society*, 123(541), 1227–1282.
- Sandford, C., Illingworth, A., & Thompson, R. (2017). The potential use of the linear depolarization ratio to distinguish between convective and stratiform rainfall to improve radar rain-rate estimates. *Journal of Applied Meteorology and Climatology*, 56(11), 2927–2940.
- Savic-Jovicic, V., & Stevens, B. (2008). The structure and mesoscale organization of precipitating stratocumulus. *Journal of the Atmospheric Sciences*, 65(5), 1587–1605.
- Stephens, G. L., L'Ecuyer, T., Forbes, R., Gettelman, A., Golaz, J. C., Bodas-Salcedo, A., et al. (2010). Dreary state of precipitation in global models. *Journal of Geophysical Research, Atmospheres*, 115, D24211. <https://doi.org/10.1029/2010JD014532>
- Sun, Y., Solomon, S., Dai, A., & Portmann, R. W. (2006). How often does it rain? *Journal of Climate*, 19(6), 916–934.
- VanZanten, M., Stevens, B., Vali, G., & Lenschow, D. (2005). Observations of drizzle in nocturnal marine stratocumulus. *Journal of the Atmospheric Sciences*, 62(1), 88–106.
- Wang, H., & Feingold, G. (2009). Modeling mesoscale cellular structures and drizzle in marine stratocumulus. Part I: Impact of drizzle on the formation and evolution of open cells. *Journal of the Atmospheric Sciences*, 66(11), 3237–3256.
- Wood, R., & Bretherton, C. S. (2006). On the relationship between stratiform low cloud cover and lower-tropospheric stability. *Journal of Climate*, 19(24), 6425–6432.
- Wood, R., Leon, D., Lebsock, M., Snider, J., & Clarke, A. D. (2012). Precipitation driving of droplet concentration variability in marine low clouds. *Journal of Geophysical Research*, 117, D19210. <https://doi.org/10.1029/2012jd018305>
- Wood, R., Wyant, M., Bretherton, C. S., Rémillard, J., Kollias, P., Fletcher, J., et al. (2015). Clouds, aerosols, and precipitation in the marine boundary layer: An arm mobile facility deployment. *Bulletin of the American Meteorological Society*, 96(3), 419–440.

- Wu, P., Dong, X., Xi, B., Liu, Y., Thieman, M., & Minnis, P. (2017). Effects of environment forcing on marine boundary layer cloud-drizzle processes. *Journal of Geophysical Research: Atmospheres*, 122, 4463–4478.
- Yamaguchi, T., & Feingold, G. (2015). On the relationship between open cellular convective cloud patterns and the spatial distribution of precipitation. *Atmospheric Chemistry and Physics*, 15(3), 1237–1251. <https://doi.org/10.5194/acp-15-1237-2015>
- Yang, F., Luke, E. P., Kollias, P., Kostinski, A. B., & Vogelmann, A. M. (2018). Scaling of drizzle virga depth with cloud thickness for marine stratocumulus clouds. *Geophysical Research Letters*, 45, 3746–3753.
- Zhou, X., Ackerman, A. S., Fridlind, A. M., & Kollias, P. (2018). Simulation of mesoscale cellular convection in marine stratocumulus. Part I: Drizzling Conditions. *Journal of the Atmospheric Sciences*, 75(1), 257–274.
- Zhou, X., Heus, T., & Kollias, P. (2017). Influences of drizzle on stratocumulus cloudiness and organization. *Journal of Geophysical Research: Atmospheres*, 122, 6989–7003.
- Zhou, X., Kollias, P., & Lewis, E. R. (2015). Clouds, precipitation, and marine boundary layer structure during the MAGIC field campaign. *Journal of Climate*, 28(6), 2420–2442. <https://doi.org/10.1175/JCLI-D-14-00320.1>